A global model of the internal magnetic field of the Moon based on Lunar Prospector magnetometer observations

Michael E. Purucker [a, *]

[a]Raytheon at Planetary Geodynamics Lab, Code 698, Goddard Space Flight Center, Greenbelt, MD 20771

[*]Corresponding Author E-mail address: michael.e.purucker@nasa.gov

Pages:23

Figures: 5

Version 2.4 16 Mar 2008

Proposed Running Head : Global lunar magnetic model

Editorial correspondence to:

Dr. Michael E. Purucker

Code 698, Planetary Geodynamics Laboratory

Goddard Space Flight Center

Greenbelt, MD 20771

Phone: 301-614-6473

Fax: 301-614-6522

E-mail address: purucker@geomag.gsfc.nasa.gov

ABSTRACT

A preliminary model of the internal magnetic field of the moon is developed using a novel, correlative technique on the low-altitude Lunar Prospector magnetic field observations. Subsequent to the removal of a simple model of the external field, an internal dipole model is developed for each pole-to-pole half-orbit. This internal dipole model exploits Lunar Prospector's orbit geometry and incorporates radial and theta vector component data from immediately adjacent passes into the model. These adjacent passes are closely separated in space and time and are thus characteristic of a particular lunar regime (wake, solar wind, magnetotail, magnetosheath) or regimes. Each dipole model thus represents the correlative parts of three adjacent passes, and provides an analytic means of continuing the data to a constant surface of 30 km above the mean lunar radius. The altitude-normalized radial field from the wake and tail regimes is used to build a model in which 99.2% of the 360 by 360 bins covering the lunar surface are filled. This global model of the radial magnetic field is used to construct a degree 178 spherical harmonic model of the field via the Driscoll & Healy sampling theorem. Terms below about degree 150 are robust, and polar regions are considered to be the least reliable. The model resolves additional detail in the low magnetic field regions of the Imbrium and Orientale basins, and also in the four anomaly clusters antipodal to the large lunar basins. The model will be of use in understanding the sources of the internal field, and as a first step in modeling the interaction of the internal field with the solar wind.

Key Words: Moon, interior; Moon, surface, Magnetic fields, Magnetospheres

1. Introduction

The internal magnetic field of the moon has been recognized since the US-Soviet exploration (Dyal et al., 1974) epoch. A global mapping of the magnetic field was performed by Lunar Prospector in 1998 and 1999 using both magnetometer and electron reflectometer instruments (Binder, 1998). The boom-mounted, 2.5 m in length, magnetometer sensor is a low-noise (6 pT RMS) triaxial fluxgate magnetometer that measures magnetic fields up to a sample rate of 18 Hz. Early efforts to isolate the internal components of the Lunar Prospector magnetic field from the magnetometer data (Hood et al., 2001) resulted in maps which covered approximately 40% or less of the moon. Maps made using the electron reflectometer approach include those of Halekas et al. (2001). Recent global maps of the internal magnetic field include those of Richmond and Hood (in press) using the vector fluxgate magnetometer, and Mitchell et al. (in press) using the electron reflectometer. Magnetic maps such as these are of use in understanding the sources of the internal field (Hood and Schubert, 1980; Nicholas et al., 2007) and in modeling the interaction of the internal field with the solar wind (Harnett and Winglee, 2003; Crider and Vondrak, 2003)

2. Data

The low-altitude (Average altitude: 30 km, Range:11-66 km above a 1737.1 km sphere) data from the vector fluxgate magnetometer covering the period between 19 December 1998 and 29 July 1999 were used in this new map. The spin-averaged observations are at 5 second intervals, during which time the spacecraft moves about 9 km along track. Using Level 1B data from NASA's Planetary Data System node,

the data were initially converted to a local tangent coordinate system with B_r positive outward, B_θ positive southward, and B_ϕ positive eastward.

3. External magnetic field model

Details of the external field model are identical with that of Nicholas et al. (2007), and are summarized here. The external field was represented as a uniform field over each satellite half-orbit, and the half orbits extend from pole to pole. The external field was determined in a least-squares sense from all three components of the vector data. There were a total of 5641 half-orbits. The external field directions determined by this approach are found to be in good agreement with the T96 model of the earth's magnetosphere (Tsyganenko, 1996) at times when the moon is in the earth's magnetic tail. The model was applied in all lunar regimes (solar wind, wake, tail, and magnetosheath) and it is expected that it will be most successful in regimes where the external field is stable over periods represented by a half-orbit (approximately 1 hour).

4. Internal model from correlative parts of adjacent passes

In the second step of this analysis, subsequent to the removal of the model of the external field, an internal space domain model is developed for each pole-to-pole half-orbit. An equivalent source formulation in spherical coordinates is used, with the magnetized lunar crust divided into blocks, each of which is assumed to have a magnetic dipole at its center. The magnetic field is derived as the gradient of a scalar magnetic potential which can be expressed as

$$V(\mathbf{r_i}) = \frac{\mu_0}{4\pi} \sum_{j=1}^{J} \mathbf{m_j} \cdot \nabla_j \frac{1}{r_{ij}}$$

where the potential V at the observation point $\mathbf{r}_i = (r_i, \theta_i, \phi_i)$ is produced by J dipoles located at $\mathbf{r_j}$ for j=1,2..J. r_{ij} is the distance between the dipole and the observation location, $\mathbf{m}_j$ is the dipole moment, and μ_0 is the vacuum permeability. This internal dipole model exploits Lunar Prospector's orbit geometry and incorporates radial and theta vector component data from three immediately adjacent passes into the model. Because the distance between the half orbits is approximately equal to their distance above the lunar surface, the magnetic field measurements are sensitive to common internal sources. These adjacent passes are separated in space by about 1 degree of longitude (30 km) at the equator, and about 1.9 hours in time. Each solution is thus characteristic of a particular lunar regime or regimes (wake, solar wind, magnetotail, magnetosheath, defined by its geocentric solar ecliptic coordinates and the sun pulse indicator), and represents the correlative part of three adjacent passes. Each solution is defined from the correlative parts of these adjacent passes, irrespective of whether plasma conditions changed during the time of these passes.

The technique is a space domain equivalent to the harmonic correlation technique of Langel (1995). That technique allowed for the isolation of a primary signal in the presence of interfering signals. The space domain implementation developed here allows for the incorporation of multiple vector components into a single solution, and serves to retain the resolution of the original data set. The dipole model also provides an analytic means of continuing the low-altitude data to an altitude of 30 km. However, the magnitude and direction of the dipoles should not be interpreted physically. In the model developed here, the dipoles are simply a tool in the analysis.

The phi vector component data was not incorporated into the solution because it is typically the most affected by unmodeled external fields, and the narrow E-W extent of the model makes its incorporation problematic. In order to include the phi vector component, the E-W extent of the modeled regions would need to be comparable to the E-W extent of the internal magnetic field feature modeled. This follows from the fact that the phi component defines the east and west edge of internal magnetic features.

Horizontal dipoles are located directly underneath the observation location of the middle pass, at a radius of 1737.1 km (the mean lunar radius). This serves to retain the resolution of the original data. The model parameters are the magnitudes of the horizontal component of $\mathbf{m}_j$. There are typically about 600 model parameters in each solution, and the data to be modeled cover a region that is almost 180 degrees (5500 km) in a N-S direction, and 2 degrees (61 km) in an E-W direction at the equator. A conjugate gradient approach is used to fit the vector observations to the magnetic dipoles in a least squares sense (Purucker et al., 1996). The design matrix was pre-conditioned to improve the rate of convergence, and each solution was iterated five times. Increasing the number of iterations increases the complexity of the solution (Langlais et al., 2004). It was found by trial and error that five iterations resulted in a solution whose complexity reflected the input data used. Other approaches to choosing the optimum smoothness include Akaike's Bayesian Information Criteria (Toyoshima et al, in press). In approximately 4% of the cases it is found that the RMS residual values increase significantly (>20%) when compared to pre-fit values. These cases are discarded, and not considered further.

Each solution is then used to calculate the radial field at an altitude of 30 km above the mean lunar radius. The low-altitude Lunar Prospector data set yielded in excess of 5000 solutions. Figure 1 shows all of the retained solutions over Mare Moscoviense from wake and tail times, next to which can be found the original radial field profiles from those same times. Richmond and Hood (in press), following Halekas et al. (2003), report the presence of a significant magnetic field feature over Mare Moscoviense, which is confirmed by this analysis.

5. Global altitude-normalized radial field from wake and tail times

The radial field solutions from wake and tail times were assembled into one degree in longitude by one-half degree in latitude bins, and a median value was determined for each bin, weighted by the altitude (Figure 2, bottom). 99.2% of the bins were populated, and the remaining unpopulated bins are in the polar regions. This data set, supplemented by the individual modeled profiles, represents the primary starting point for interpretations of the internal field. These data are available in digital form at http://core2.gsfc.nasa.gov/research/purucker/moon2007 and could be used, for example, to refine the selection criteria. A similar exercise was performed for radial field solutions from solar wind times (Figure 2, top), and a comparison with the wake and tail time model shows a significant diminution of amplitude. This is interpreted to be a consequence of the formation of mini-magnetospheres during solar wind times, resulting in a much greater variability in the internal field (e.g. Kurata et al., 2005). In order to produce a spherical harmonic model of the lunar magnetic field, a model is needed that has data in all bins, and hence we fit the observations with an adjustable

tension (T=0.25 was used, and is commonly used for potential field data) continuous curvature surface (Wessel and Smith, 1998).

6. Spherical harmonic model of the vector magnetic field

The one degree by one-half degree radial field determined for the entire moon (Figure 2, bottom) can be utilized to construct a spherical harmonic potential to degree and order 178 via the Driscoll & Healy sampling theorem (Driscoll, 1994). This potential is expressed as

$$V = a\sum_{n=1}^{178}\left(\frac{a}{r}\right)^{n+1}\sum_{m=0}^{n}\left(g_n^m\cos(m\phi)+h_n^m\sin(m\phi)\right)P_n^m(\cos\theta)$$

where a is the mean radius of the Moon, r is the radial distance of the observation from the center of the Moon, ϕ denotes longitude and θ colatitude, $P_n^m(\cos\theta)$ are the Schmidt quasi-normalized associated Legendre functions of degree n and order m, and the g_n^m and h_n^m are the estimated spherical harmonic coefficients. The radial, theta, and scalar components computed from this model at the same altitude as Figure 2 are shown in Figure 3. Notice the smoothing that has occurred relative to Figure 2, especially at high latitudes. Polar regions are considered the least reliable part of the new map, although little or no evidence is seen suggesting the presence of a lunar wake boundary in the observations (Halekas et al., 2005). The spherical harmonic model, available at http://core2.gsfc.nasa.gov/research/purucker/moon2007, can be used to place a minimum estimate on the strength of the internal field at a specified altitude, latitude, and longitude. Such an estimate may prove useful in modeling the interaction of the internal field with the solar wind field (Harnett and Winglee, 2003).

From this spherical harmonic model, the Lowes-Mauersberger power spectra (Lowes, 1966) at the Moon's surface (Figure 4) is calculated, and compared with recent determinations of the power spectra of the magnetic field of Mars and the Earth. This power spectra is defined as the mean square magnetic field described by harmonics of degree *n*, averaged over a spherical surface of radius *a* containing the sources. The gradual increase in power beginning at about spherical harmonic degree 150 is interpreted as the onset of significant noise in the solution, and the solution is therefore truncated at degree 150.

7. Discussion

Recent maps of the crustal magnetic field of the moon are available from both the electron reflectometer (Mitchell et al., in press) and the magnetometer (Richmond and Hood, in press). Figure 5 shows the scalar fields from these maps compared with the scalar map made from the spherical harmonic degree 150 model. The long-wavelength highs and lows agree amongst all three maps, but there are many differences in the small scale features, and in the magnitude of features. The major lows associated with the Imbrium (I) and Orientale (O) basins are seen in all maps, although the Orientale low in the Richmond and Hood map is subdued. The electron reflectometer (ER) map represents estimates of surface magnetic field magnitude, while the magnetometer maps represent fields at 30 km altitude. The ER map was determined utilizing measurements of adiabatically reflected electrons to remotely sense crustal magnetic fields at the surface. This map is completely corrected for the effects of near-surface electric field, which also reflect electrons. The surface location for each observation from orbit is determined by a straight line magnetic field trace. The magnitude for moderate fields (a few nT to tens of nTs) is more reliable than

those for higher fields. The magnitudes determined using the ER technique are lower limits.

While the ER and magnetometer maps match up well qualitatively, we do not expect them to correspond exactly, since the ER map should have more sensitivity to localized incoherent magnetization at the surface, while the magnetometer map should have more sensitivity to more coherent and/or deep-seated magnetization. The two magnetometer maps exhibit a linear correlation coefficient (Press et al., 1992) of 0.64. A correlation coefficient of 1 represents perfect correlation, 0 represents no correlation, and –1 represents perfect anti-correlation. The ER map shows a correlation coefficient of 0.47 with the Richmond and Hood (in press) map, and of 0.61 with the map developed in this study. At lower field magnitudes, the Richmond and Hood (in press) map shows more data gaps and north-south features that closely parallel the track lines.

Comparisons can also be undertaken between the magnetic fields measured during the Apollo program and the recent Lunar Prospector models. Quantitative comparison is hindered because these early data were never sufficient to make a global map, and by the difficulty of reading the primary tapes. It has been known since analysis of the Apollo data that curvilinear features (often called swirls) like those in Reiner Gamma and Descartes were associated with strong magnetic fields (Hood et al., 1979). A map of the magnitude of the Reiner Gamma anomaly was included in the Hood et al. (1979) paper. That map has not been altitude normalized, but it is reported that the altitude of the observations is about 20 km directly above the anomaly. The field peaks at 10.5 nT directly above the Reiner Gamma feature at 7.5 degrees North, 59 degrees West latitude. In contrast, the field at 30 km altitude from the current model, and from the Richmond and Hood model (in press) is about 16 nT. The location of the

peak anomaly and its overall trend (NE) is unchanged from the Apollo observations, providing additional confidence in the Lunar Prospector results. The calibration of the Lunar Prospector magnetometer is considered to be significantly better that of the Apollo magnetometers (Binder et al. 1998), hence the difference in field magnitudes over Reiner Gamma is not considered unusual.

At degrees in excess of 17, magnetic fields from the Earth (Sabaka et al., 2004), Moon, and Mars (Langlais et al., 2004) are all of crustal origin, and the magnitude of the difference in the power spectra, spanning almost eight orders of power, illustrates the large disparity that must exist in the remanence carriers that host the magnetic field. However, it is intriguing that the shape of the lunar and Martian power spectra is very similar, suggesting that although the remanence carriers may be very different, the source depths on the two bodies may be very similar (Voorhies et al., 2002). The lunar spectra may also serve as a model for the Earth's unknown low-degree crustal power spectra (Jackson, 1996).

8. Conclusion

A preliminary model of the internal magnetic field of the moon is developed that exploits Lunar Prospector's orbit geometry to extract the common signal from immediately adjacent passes. The error levels of this map are set by the inherent accuracy of the Lunar Prospector magnetometer (<0.5 nT). The higher resolution views achieved by this study, when compared to previous studies (Hood et al., 2001; Richmond and Hood, in press), are largely the result of the correlative approach to signal extraction, which isolates common signals in the presence of signals from unmodeled sources, originating most commonly from temporal variability of the

external magnetic field. This will be successful to the extent that the modeled internal signal differs in character from the signal from unmodeled sources.

Acknowledgments

I would like to thank NASA's Discovery Data Analysis Program for support of this research, T.J. Sabaka for the external field model, M. Wieczorek for SHTOOLS, and P. Wessel and W. Smith for GMT. Comments by N. Richmond, M. Wieczorek, J. Halekas, B. Langlais, and an anonymous reviewer were very helpful.

References

Binder, A.B., 1998, Lunar Prospector: Overview. Science 281, 1475-1476.

Crider, D.H., Vondrak, R.R, 2003. Space weathering effects on lunar cold trap deposits. J. Geophys. Res 108, 5079, doi:10.1029/2002JE002030.

Driscoll, J.R., Healy, D.M., 1994. Computing Fourier transforms and convolutions on the 2-sphere. Adv App. Math. 15(2), 202-250.

Dyal, P., Parkin, C.W., Daily, W.D., 1974. Magnetism and the interior of the Moon. Rev. Geophys. Space Phys. 12, 568-591.

Halekas, J.S., Mitchell, D.L., Lin, R.P., Frey, S, Hood, L.L, Acuna, M.H., Binder, A.B., 2001. Mapping of crustal magnetic anomalies on the lunar near side by the Lunar Prospector electron reflectometer. J. Geophys. Res. 106, 27841-27852.

Halekas, J.S., Lin, R.P, Mitchell, D.L., 2003, Magnetic fields of lunar multi-ring impact basins. Meteor. Planet. Sci. 38, 565-578.

Halekas, J.S., Bale, S.D., Mitchell, D.L., Lin, R.P., 2005, Electrons and magnetic fields in the lunar plasma wake, J. Geophys. Res. 110, A07222, doi: 10.1029/2005GL022627.

Harnett, E.M, Winglee, R.M., 2003. 2.5D fluid simulations of the solar wind interacting with multiple dipoles on the surface of the Moon. J.Geophys Res 108, 1088, doi:10.1029/2002JA009617.

Hood, L.L., Coleman, P.J., Jr, Wilhelms, D.E., 1979, Lunar nearside magnetic anomalies, in Lunar & Planetary Sci. Conf., 10th, Houston, TX, March 19-23, 1979, Proceedings, Volume 3 (A80-23677 08-91) New York, Pergamon Press, Inc., 2235-2257.

Hood, L.L, Schubert, G. 1980, Lunar magnetic anomalies and surface optical properties. Science 208, 49-51.

Hood, L.L, Zakharian, A., Halekas, J., Mitchell, D.L., Lin, R.P., Acuna, M.H., Binder, A.B. 2001. Initial mapping and interpretation of lunar crustal magnetic anomalies using Lunar Prospector magnetic data. J. Geophys. Res. 106, 27825-27840.

Jackson, A., 1996. Bounding the long wavelength crustal magnetic field. Phys. Earth Plan. Int. 98, 283-302.

Kurata, M., Tsunakawa, H., Saito, Y., Shibuya, H., Matsushima, Shimizu, H. 2005. Mini-magnetosphere over Reiner Gamma magnetic anomaly region on the Moon. Geophys. Res. Lett 32, L24205, doi:10.1029/2005GL024097.

Langel, R.A., 1995. An investigation of a correlation/covariance method of signal extraction. J. Geophys. Res. 100, 20137-20157.

Langel, R.A.,Hinze W.J., 1998. The magnetic field of the Earth's lithosphere. Cambridge Univ. Press, Cambridge, UK.

Langlais, B., Purucker, M, Mandea, M., 2004. Crustal magnetic field of Mars. J. Geophys. Res. 109, E02008, doi:10.1029/2003JE002048.

Lowes, F.J, 1966. Mean square values on the sphere of spherical harmonic vector fields. J. Geophys. Res. 71, 2179.

Mitchell, D.L., Halekas, J.S., Lin, R.P., Frey, S. Hood, L.L., Acuna, M.H., Binder, A., in press. Global mapping of Lunar crustal magnetic fields by Lunar Prospector, Icarus.

Nicholas, J.B., Purucker, M.E., Sabaka, T.J., 2007. Age spot or youthful marking: Origin of Reiner Gamma. Geophys. Res. Lett. 34, L02205, doi:10.1029/2006GL027794.

Press, W.H., Teukolsky, S.A., Vetterling, W.T, Flanney, B.P., 1992. Numerical Recipes in Fortran : The Art of Scientific Computing, 2nd ed., Cambridge Univ. Press, Cambridge, U.K.

Purucker, M., Sabaka, T., Langel, R., 1996. Conjugate gradient analysis: A new tool for studying satellite magnetic data sets. Geophys. Res. Lett. 23, 507-510.

Richmond, N.C., Hood, L.L., Halekas, J.S., Mitchell, D.L., Lin R.P., Acuna, M., Binder A.B., 2003, Correlation of a strong lunar magnetic anomaly with a high-albedo region of the Descartes mountains, Geophys. Res. Lett. 30(7), 1395, doi:10.1029/2003GL016938.

Richmond, N.C., Hood, L.L., in press.. A preliminary global map of the vector lunar crustal magnetic field based on Lunar Prospector magnetometer data, J. Geophys. Res- Planets, doi:10.1029/2007JE002933

Sabaka T.J., Olsen, N., Purucker, M. E., 2004. Extending comprehensive models of the Earth's magnetic field with Orsted and CHAMP data. Geophys. J. Int. 159, 521-547, doi : 10.1111/j.1365-246X.2004.02421.x

Toyoshima, M., Shibuya, H., Matsushima, M., Shimizu H., Tsunakawa, H., in press. Equivalent source mapping of the lunar crustal field using ABIC, Earth Planets Space.

Tsyganenko, N.A., 1996. Effects of the solar wind conditions onthe global magnetosphere configuration as deduced from data-based field models. Eur. Space Agency Spec. Publ.. ESA SP-389, 181-185.

Voorhies, C.V., Sabaka, T.J., Purucker, M., 2002. On magnetic spectra of Earth and Mars. J. Geophys. Res. 107, 5034, doi :10.1029/2001JE001534.

Wessel, P., Smith, W., 1998. New improved version of Generic mapping tools released, EOS transactions of the American Geophysical Union 79, 579.

Figure captions

Figure 1. Lunar Prospector radial field profiles (right) and internal models (left) acquired during wake and tail times centered over Mare Moscoviense. On the right are the profiles from which only an external field model has been removed. On the left are altitude-normalized (30 km above the lunar mean radius) internal models built from the profiles on the right. Reds indicate positive fields, blues are negative. These models extract the correlative parts of adjacent passes, and utilize both the radial and theta components of the vector magnetic field in a dipole basis, conjugate gradient, least-squares approach. Cylindrical equidistant projection.

Figure 2. Global radial median magnetic field maps at an altitude of 30 km above the lunar mean radius of the near- and far-sides of the Moon, during periods when the Moon is protected from the solar wind (bottom) and when it is the solar wind (top), determined using the correlative parts of adjacent passes. The maximum and minimum field values are shown on the right and left ends of the color scale. Lambert equal area projection.

Figure 3 Global spherical harmonic model of the lunar magnetic field at an altitude of 30 km above the lunar mean radius. From top to bottom: Scalar magnitude, theta component, and radial component fields. Near side maps are shown on the left, far side on the right. D locates the Descartes anomaly of Richmond et al. (2003). The maximum and minimum field values are shown on the right and left ends of the color scale. Lambert equal area projection.

Figure 4. Lowes-Mauersberger power spectra at the Moon's surface, compared with recent determinations of the power spectra of the magnetic field of the Earth (Sabaka et al., 2004) and Mars (Langlais et al., 2004). R_n is the mean square amplitude of the magnetic field produced by harmonics of degree n.

Figure 5. Magnitude of magnetic field measured by the Magnetometer and Electron Reflectometer (ER) instruments onboard Lunar Prospector. All measurements are based on low-altitude LP data from wake and tail times. The ER data are binned on 1 degree centers, and boxcar smoothed over 3 x 3 degrees. The ER fields are estimated at the lunar surface, the magnetometer at 30 km altitude. nT=nanoTeslas. The two magnetometer measurements have the same scale. The ER measurements have a different scale because they are measured on the surface. The symbols I and O on the maps locate the approximate center of the Imbrium and Orientale basins.

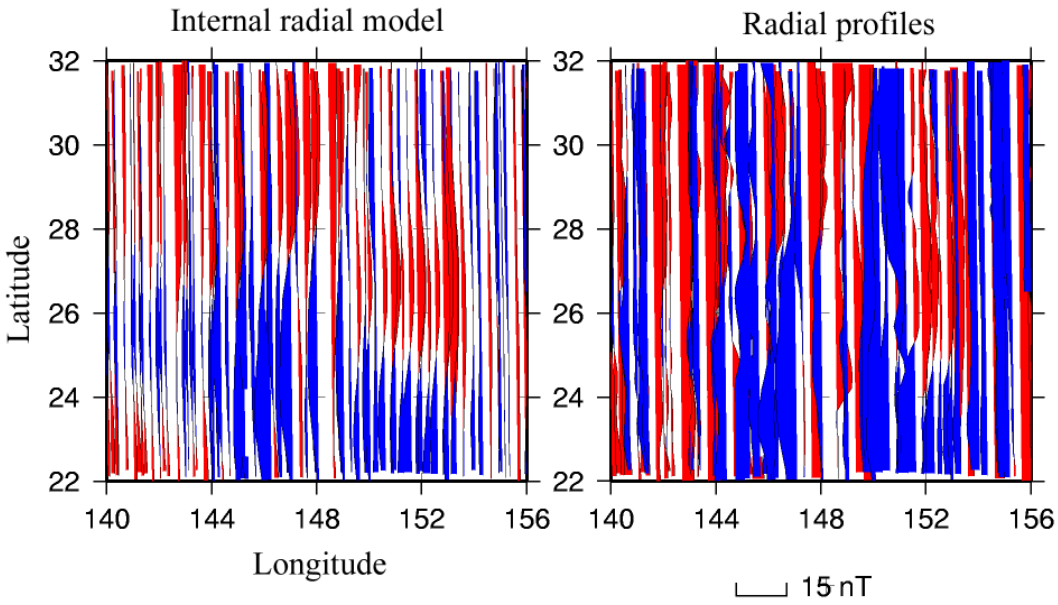

Figure 1 Purucker,Global lunar magnetic model

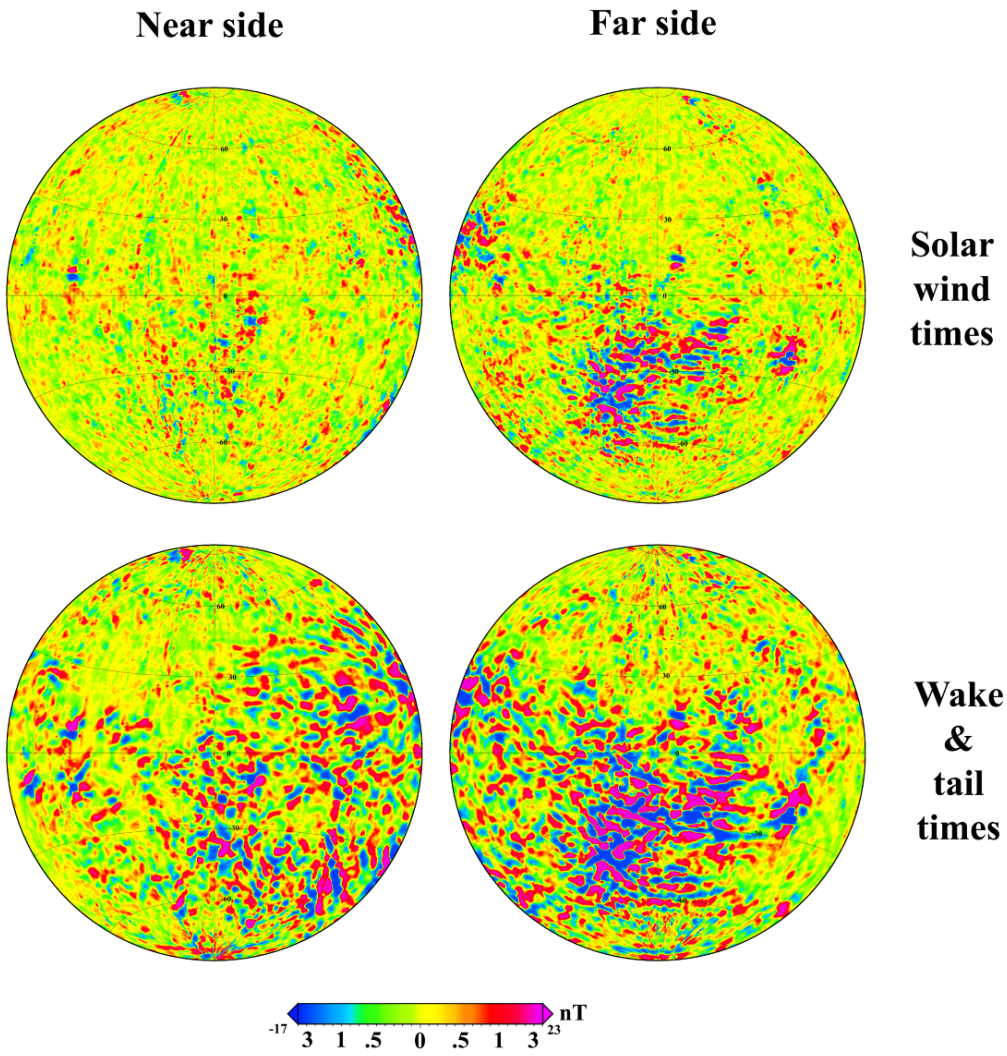

Figure 2. Purucker. Global lunar magnetic model

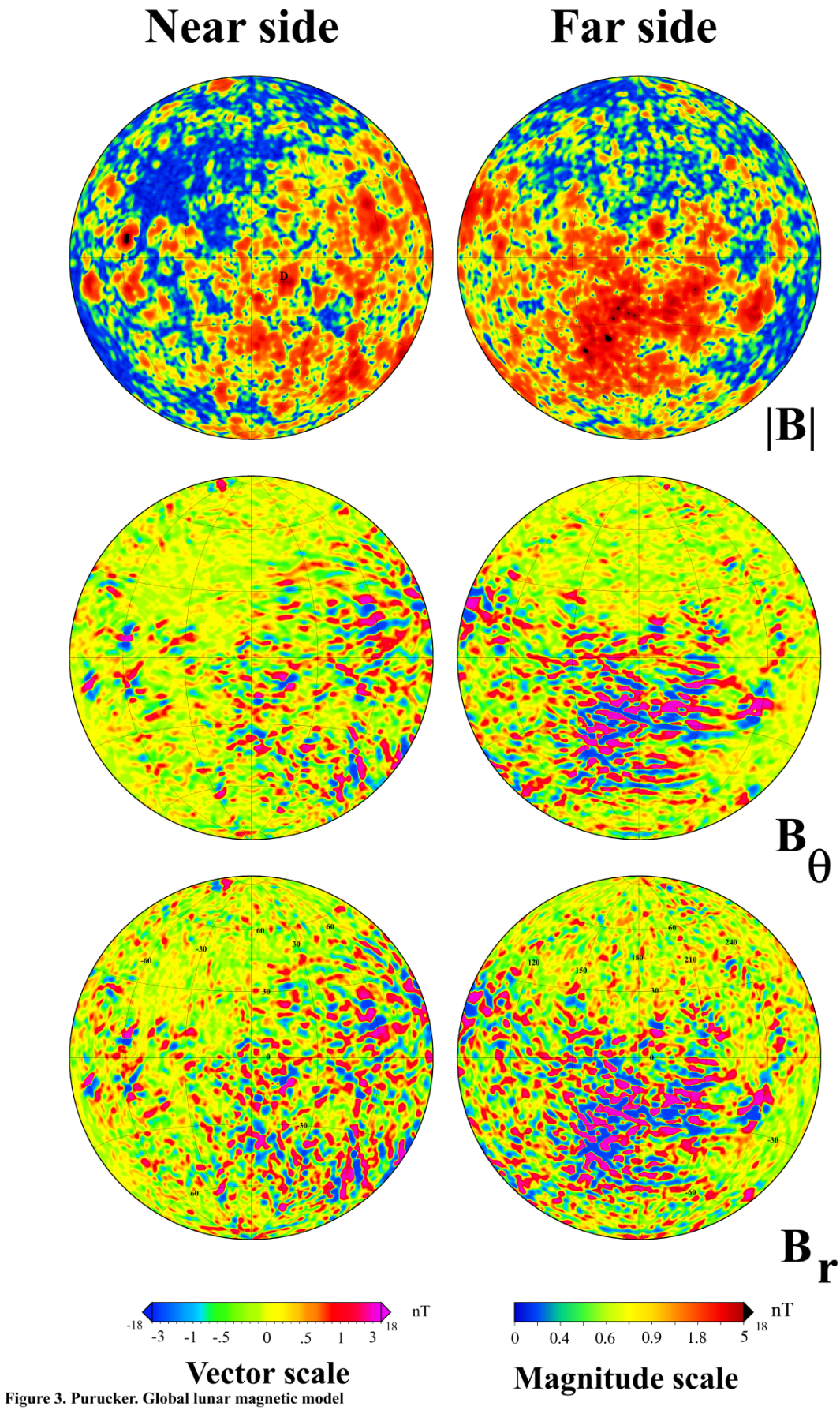

Figure 3. Purucker. Global lunar magnetic model

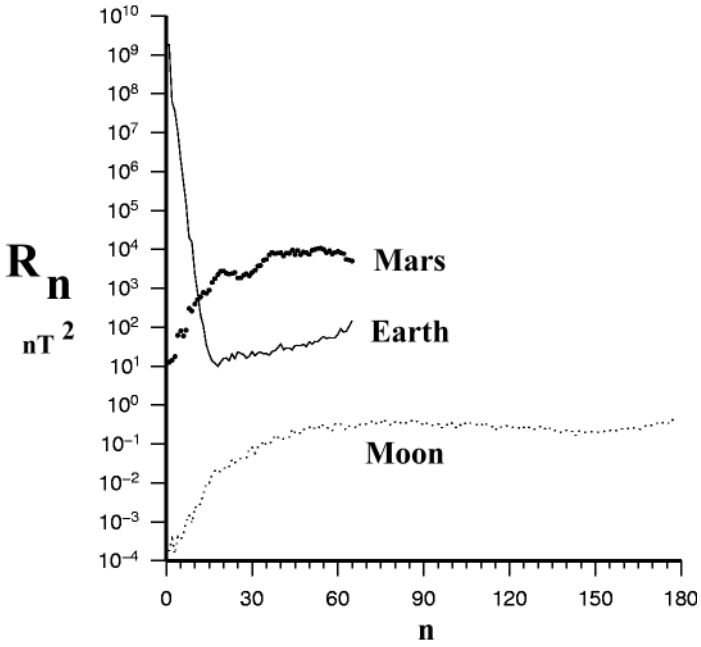

Figure 4, Purucker, Global lunar magnetic model

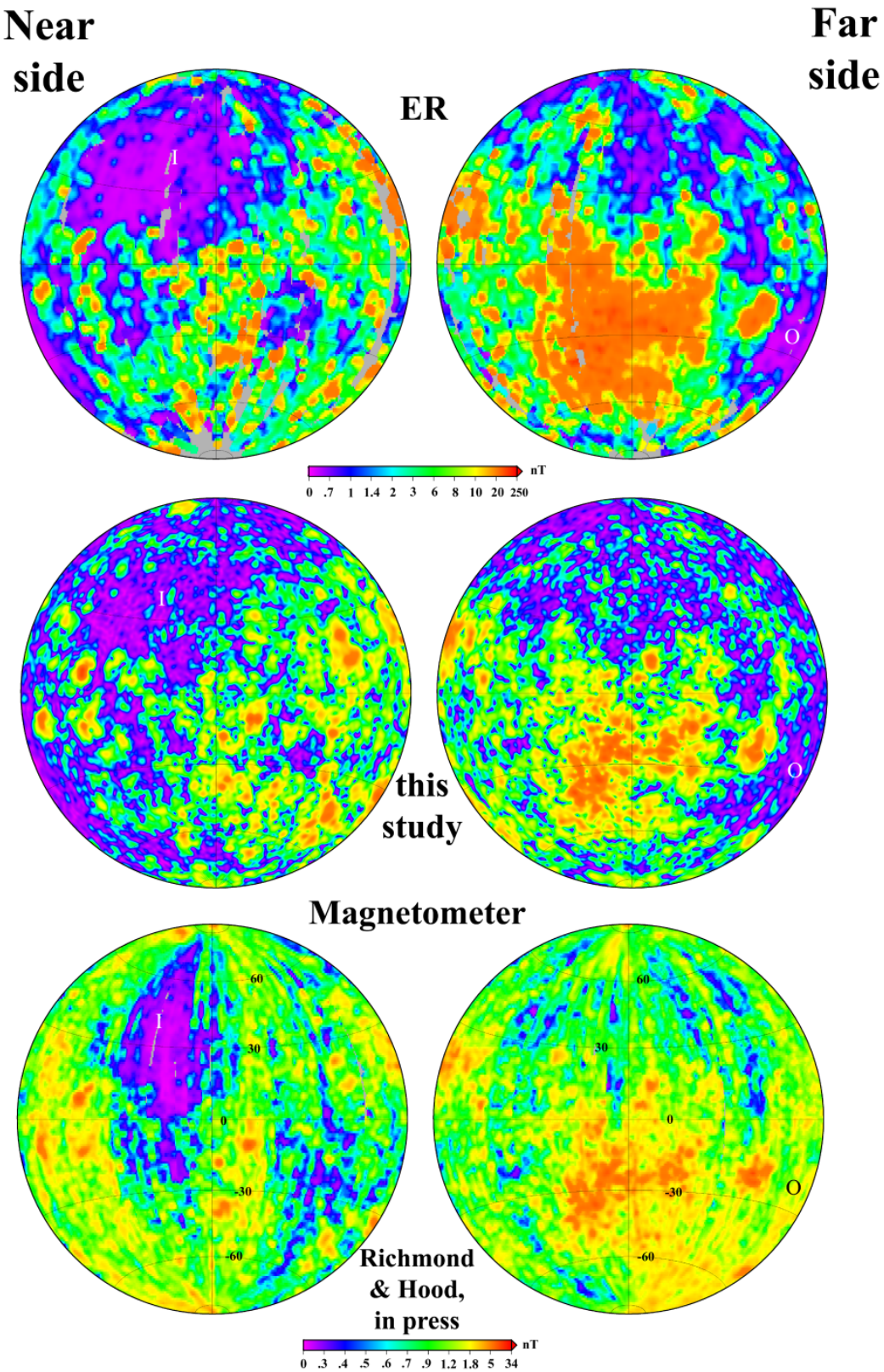

Figure 5, Purucker, Global lunar magnetic model